A novel approach to enhance defect detection in wire arc additive manufacturing parts using radiographic testing without surface milling

Mahjoub El Mountassir[1] · Didier Flotte[2] · Slah Yaacoubi[1] · Eric Riff[2] · Morgan Ferrari[2] · Daniel Chauveau[3] · Clément Bourlet[4] · Sacha Bernet[5]

Abstract

The wire arc additive manufacturing (WAAM) process is gaining popularity in industrial production due to its ability to manufacture large, customized, and complex shapes. However, because of the lack of quality assurance standards in this field, non-destructive testing (NDT) methods are required to evaluate the quality of the produced parts. Radiography testing is a good candidate for that purpose, but the surface roughness of the product being tested can lead to difficulties in the interpretation of the obtained image, which could result in unseen defects. To overcome this challenge, we propose, in this study, a novel approach for improving defect detectability using 3D laser scanning and an appropriate mathematical formulation. We first tested this approach on a weld bead and then verified it on different healthy and defective WAAM parts. In all cases, the created defects were successfully detected. Besides, the effect of surface roughness was significantly reduced. A special attention should, however, be paid to the scattering noise in the radiographic image.

Keywords Wire arc additive manufacturing, · Quality assurance · Radiographic testing · 3D laser scanning

Introduction

Wire arc additive manufacturing (WAAM) allows the manufacturing of complex-shaped parts that are difficult to produce using conventional manufacturing processes (*i.e.*, machining, forging, casting, etc.) (Cunningham et al., 2018; Derekar,

✉ Mahjoub El Mountassir
m.elmountassir@isgroupe.com

✉ Slah Yaacoubi
s.yaacoubi@isgroupe.com

1 Equipe Monitoring et Intelligence Artificielle, Institut de Soudure, 4 Boulevard Henri Becquerel, 57970 Yutz, France

2 Equipe CND Avancés, Institut de Soudure, 4 Boulevard Henri Becquerel, 57970 Yutz, France

3 Institut de Soudure Industrie, 90 Rue des Vanesses, 93420 Villepinte, France

4 Equipe Soudage Arc, Institut de Soudure, 4 Boulevard Henri Becquerel, 57970 Yutz, France

5 Holo3 Métrologie Optique, 7 rue du Général Cassagnou, 68300 Saint-Louis, France

2018; Williams et al., 2016). It can also simplify assemblies by reducing the number of required parts. This results in material savings and thus, part-lightening, which is very important for industries such as aerospace and automotive (Omiyale et al., 2022). However, as with any manufacturing process, the presence of internal defects can be problematic. It is therefore necessary to assess the quality of these parts. Non-destructive testing (NDT) and monitoring techniques can be used to reach this aim (Chen et al., 2021).

Monitoring the welding parameters (for example, current and voltage) is easy to implement and can help in identifying manufacturing deviations, particularly the shift in weld pool position, as proposed by Li et al. (2022). Nevertheless, there remains a need for further investigation to ascertain the potential correlation, if any, between variations in these parameters and prevalent defects in WAAM such as cracks, porosities, and lack of fusion (Chen et al., 2021). Concerning surface defects, several approaches have been proposed, including the utilization of a laser profilometer (Huang et al., 2022) and a high dynamic range (HDR) camera (Lee et al., 2021). Shin et al. (2023) have successfully integrated the data collected from this latter with the welding parameters to effectively

detect geometric irregularities. In addressing similar defects, both on the surface and subsurface levels, He et al. (2021) have introduced a novel NDT method called magneto-optical imaging. Recently, some researchers have focused on the use of acoustical techniques, employing microphones positioned near the manufacturing torch (Bevans et al., 2023; Ramalho et al., 2022; Surovi & Soh, 2023). However, the presence of a noisy environment poses challenges in discerning pertinent defect-related information from the background manufacturing activity.

Alternatively, different research studies have proven the efficiency of ultrasound and radiography testing for the detection of defects in WAAM (Chauveau, 2018; Honarvar & Varvani-Farahani, 2020; Javadi et al., 2019; Lopez et al., 2018; Zimermann et al., 2021). For example, Chabot et al. (2020) applied phased array (PA) ultrasonic testing to WAAM aluminum alloy parts. They have demonstrated that this method enables the detection and characterization of porosity defects. Nevertheless, the use of ultrasound NDT techniques can be costly and time-consuming since additional machining of the WAAM part surface is required. This is because ultrasound sensors are not adapted to irregular surfaces (Ma et al., 2020). Radiographic testing can be performed without milling the surface of the WAAM part. However, there is another problem here, also related to the surface condition of these parts. Explicitly, the surface roughness of the WAAM part will generate a variation in the grey level in the radiographic image that could hinder the detection of defects. To the best knowledge of the authors, this issue has never been addressed in the literature. Hence, we propose, in this paper, an approach to overcome the said issue, and so facilitating the interpretation of radiographic testing images and enhancing defect detectability. This approach includes but not limited to 3D laser scanning measurements. The combination of radiographic image and 3D laser profilometry data should help to completely erase the effects of the surface roughness. Therefore, only information about the presence of defects will be highlighted.

The reminder of this paper is as follows: the next section is devoted to background where principles of radiographic testing and 3D laser scanning are briefly explained. This helps to understand Sect. "Approach", which concerns the proposed approach. Sect. "Applications" presents some examples of applications. Finally, Sect. 5 concludes the paper and suggests future works.

Background

Radiographic testing

Radiographic testing (RT) is an NDT technique where a radiation source emits high-energy photons, usually X-rays,

through a test specimen into a detector (Bossi et al., 2002). An internal representation of the specimen, in the form of a grey level image, is generated due to differences in thickness, which impact the absorption rate of the X-ray flux. Mathematically, the relation between the thickness and the absorption rate can be approximated as follows:

$$I = I_0 e^{-\mu\tau}, \tag{1}$$

where I is the transmitted X-ray flux through the specimen, I_0, the incident X-ray flux, μ, the absorption coefficient, and τ, the crossed thickness.

From Eq. (1), it is clear that for a relatively small variation of the thickness τ, the relationship between the grey level in the radiographic image and the thickness can be approximated by a linear function. This characteristic is the cornerstone of the proposed approach.

3D laser scanning

3D laser scanning is an important technique used to characterize the geometry of a given specimen. In this study, two commercial syste ms were used. The first one, which is shown in Fig. 1a, is provided by Micro-Epsilon Company. This system is easy to use and allows rapid and accurate measurements. However, it has limited degrees of freedom, and thus, it cannot be used for the characterization of complex-shape specimens. For this reason, an advanced measuring system called Hexagon absolute arm (Fig. 1b) was used. This second system is composed of a laser source and a camera. In this case, the measurement is ensured using the triangulation principle (Munaro et al., 2015) (*i.e.*, the camera, the laser source, and the measurement point form a triangle). Consequently, knowing the distance and the angle between the camera and the laser source, the distance to the scanned point can be determined (Yaacoubi et al., 2019).

Approach

Overview and challenges

The general idea of the proposed approach to mitigate the effects of the surface roughness in the radiographic image is presented in Fig. 2. Let's consider a specimen that contains some defects. This specimen will be subjected first to radiographic testing and then to 3D laser scanning to measure its thickness at each point. Afterthat, these thicknesses will be converted to gray level to obtain a virtual radiographic image of the specimen. Ideally, by subtracting the original radiographic image from the virtual radiographic image, the surface roughness will be removed, and hence defects will be further highlighted.
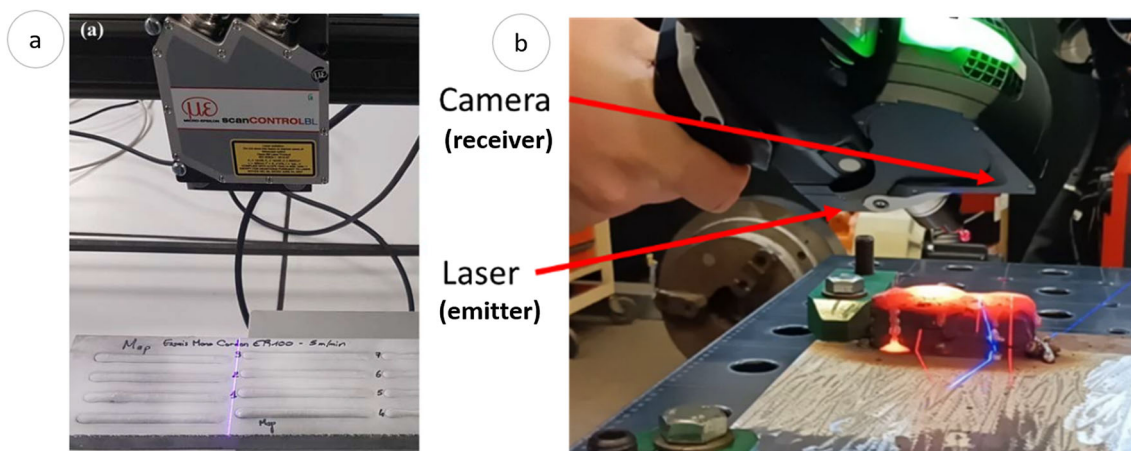
Fig. 1 3D laser scanning: micro-epsilon laser tool (**a**), and Hexagon absolute arm (**b**)
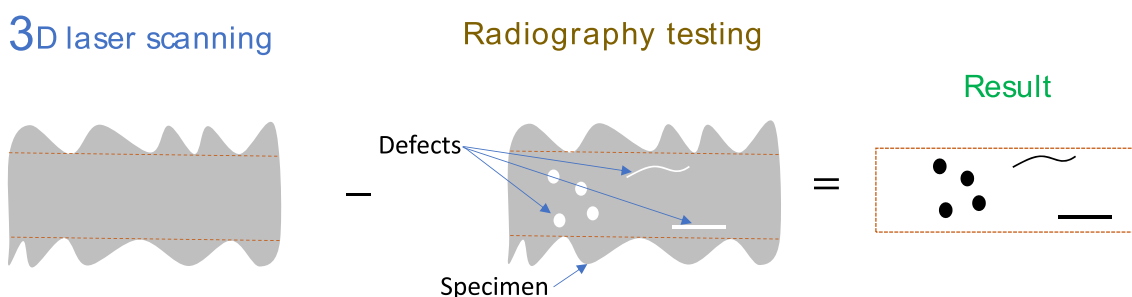

Fig. 2 Schematic illustration of the proposed approach

Nevertheless, it is not easy, in reality, to obtain this result because of many challenges. First, the approach relies on the hypothesis that there is a linear relationship between the X-ray density level and the thickness. This hypothesis is, however, only true for a small variation of thickness. Second, because of the divergence of the X-ray beam, the crossed path by the X-ray flux is different from the thickness measured via a 3D laser scanner. Third, X-ray flux is not uniform, which means that the same thickness would be represented by different density levels. Finally, the scattering phenomena are unpredictable. The second and third challenges can be faced, as will be seen later on, but the scattering phenomena are difficult to deal with.

Conversion from thickness to grey level

Finding the relationship between the thickness and the grey level is the most important step of the proposed approach. To do so, a step wedge, as shown in Fig. 3a, must be used. Radiographic testing should be applied on this step wedge using the same operational conditions as for the specimen being tested (Fig. 3b). The obtained result helps to determine the grey level that corresponds to each level of the step wedge (*i.e.*, in terms of thickness). It should be noted here that using the radiographic image of a step wedge is a common practice

to assess the depth of the detected defects in radiographic testing (Lee & Kim, 2005; Misale et al., 2009; Wang & Evans, 2021). In the present work, a linear regression is performed, as shown in Fig. 3(c). This function (also said model) can be written as:

$$\text{Grey level} = \alpha\tau + \beta, \tag{2}$$

where α and β are the regression coefficients.

It is important to note that the choice of the step wedge (*i.e.*, minimum and maximum thickness) should depend on the range of variation of the specimen thickness since the established linear model can provide a good estimate within the range of the data used to train the model, but it may not predict accurately outside that range.

To evaluate the goodness of fit of the found linear regression model, the determination coefficient R^2 is generally calculated (Cheng et al., 2014). It ranges from 0 to 1. The closer to zero is R^2, the more the data points spread far from the regression line. On the contrary, the closer to 1 is R^2, the more the cloud of points fits the regression line. Mathematically, R^2 is defined by the following equation:

$$R^2 = 1 - \frac{\sum_{i=1}^{n}(y_i - \hat{y}_i)^2}{\sum_{i=1}^{n}(y_i - \overline{y})^2}, \tag{3}$$
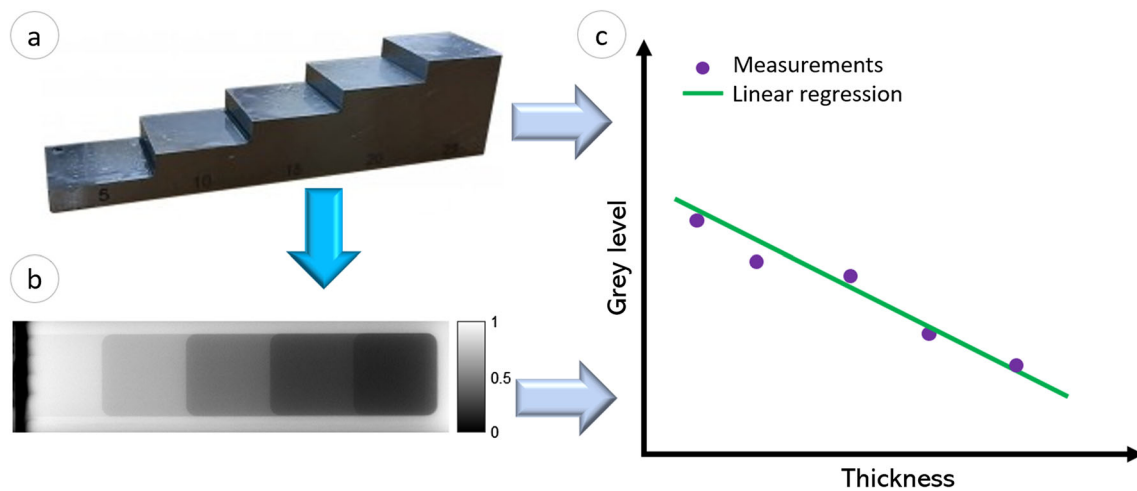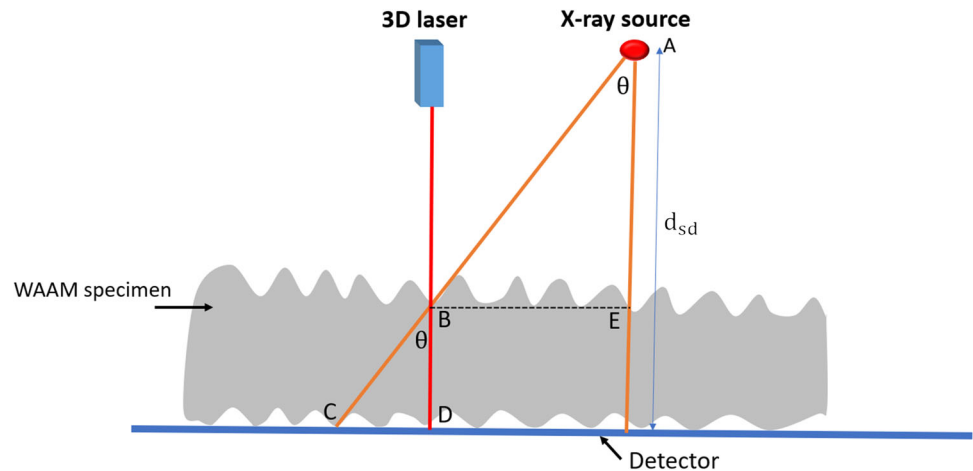
Fig. 3 Methodology to establish the relationship between the thickness and the grey level: step wedge (**a**), its radiography image (**b**), and linear regression (**c**)

Fig. 4 Schematic illustration of the thickness measurement correction, **d$_{sd}$** is the distance separating the X-ray source from the detector

where n is the number of measurements, y_i is the actual value of the measure i, $\widehat{y}_i$ is its estimated value and $\overline{y}$ is the mean of the measured values **y**.

Thickness correction

Now, before using the linear regression model, found in the previous section, to convert thickness values into gray levels, the measured thickness by the 3D laser scanner must be corrected. An illustration is shown in Fig. 4. Actually, the thickness [BD] measured by 3D laser scanning does not really correspond to the crossed path by the X-ray flux [BC]. It is worth noting that this step is very important to get precise measurement. For example, in the case of pipeline testing, it was shown that this phenomenon led to an overestimation of the wall thickness (Tennakoon, 2005).

To address this issue, the angle θ is first calculated using the following expression:

$$\theta = \tan^{-1}\left(\frac{BE}{d_{sd} - BD}\right), \tag{4}$$

where d_{sd} is the distance between the X-ray source and the detector. The distance [BE] can be calculated for each position of the 3D laser scanner by knowing the resolution of displacement (noted as Δp).

Besides, the expression of the crossed path by the X-ray flux is given by:

$$BC = \frac{BD}{\cos\theta}, \tag{5}$$

By substituting the expression of the angle θ in Eq. 5, the value of the crossed path by the X-ray flux can be obtained.
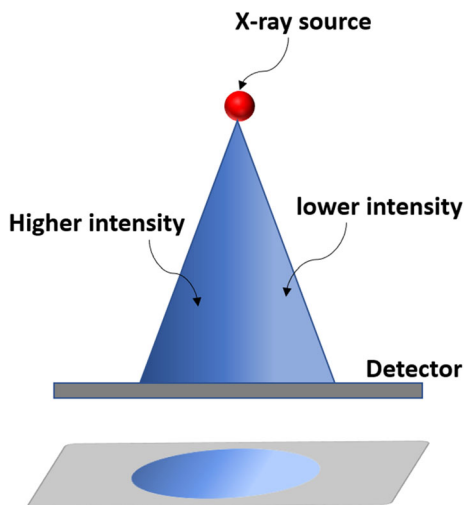
Fig. 5 Illustration of the Heel effect

X-ray flux correction

Another issue, related this time to the radiographic image, is the non-uniformity of the X-ray flux, which is also known as the anode Heel effect (Salleh et al., 2014). Explicitly, the radiation intensity of the X-ray source is higher near the cathode, leading to a brighter image on that side (Kusk et al., 2021). This phenomenon is illustrated in Fig. 5, which shows a variation in the X-ray beam intensity across the detector surface, caused by the said effect.

To better assess this effect, a steel sheet with constant thickness was subjected to radiographic testing. The obtained radiographic image is presented in Fig. 6a. A row and column were extracted and shown in Fig. 6b and c, respectively. This result shows that even though the thickness of the sheet is constant (30 mm in this case), the grey level is variable; a trend can be clearly remarked. However, the proposed method relies on the hypothesis that there is a one-to-one correspondence (*i.e.*, bijective function) between the grey levels in the radiographic image and the values of the thickness of the specimen. For this reason, a correction task is required.

In the literature, different solutions were proposed to mitigate or cancel out this effect (Behiels et al., 2002; Do Nascimento et al., 2008; Nazemi et al., 2019; Pawluczyk & Yaffe, 2001). However, these solutions are generally based on complex mathematical models, such as artificial neural networks or additional hardware. In our case, since the observed trend can be interpolated by a polynomial function, to solve this issue, each row $\mathbf{r_i} = (r_{ij})_{1 \le j \le N}$, $1 \le i \le M$ of the X-ray image is fitted using a quadratic polynomial function, which can be mathematically expressed as:

$$P(x) = \sum_{k=0}^{2} a_k x^k = a_0 + a_1 x + a_2 x^2, \quad x \in \mathbb{R} \tag{6}$$

The coefficients a_k, $k = 0, 1, 2$ can be determined by minimizing an error function that measures the misfit between the function P and the raw data (Thompson & Balch, 1988), as follows:

$$\hat{\mathbf{a}} = \min_{a_k} \frac{1}{2} \left(\sum_{j=1}^{N} P(x_j) - r_{ij}^2 \right), \tag{7}$$
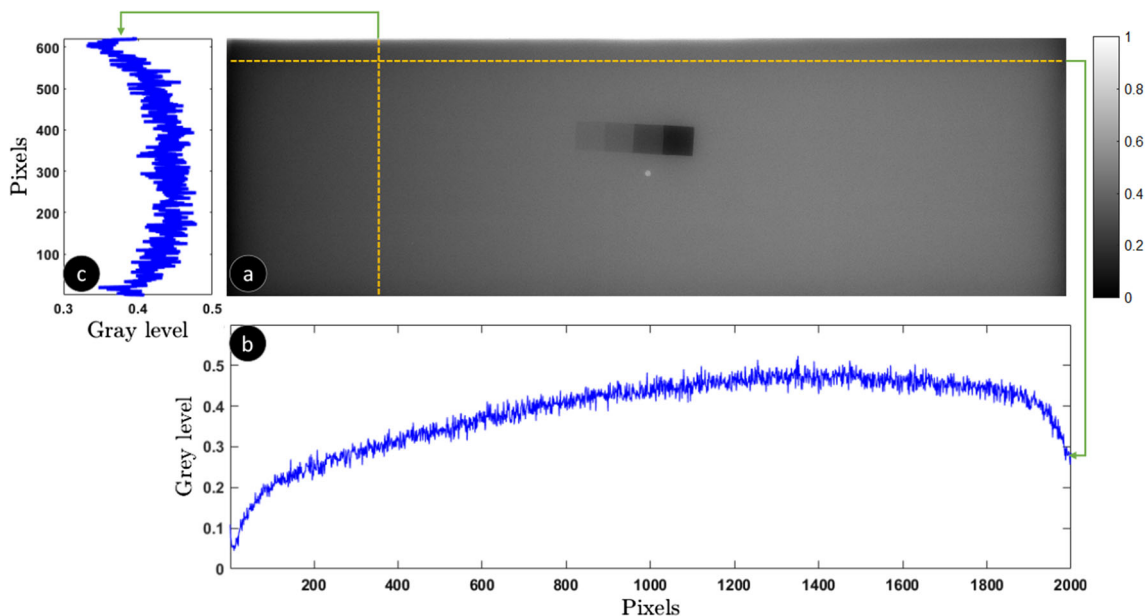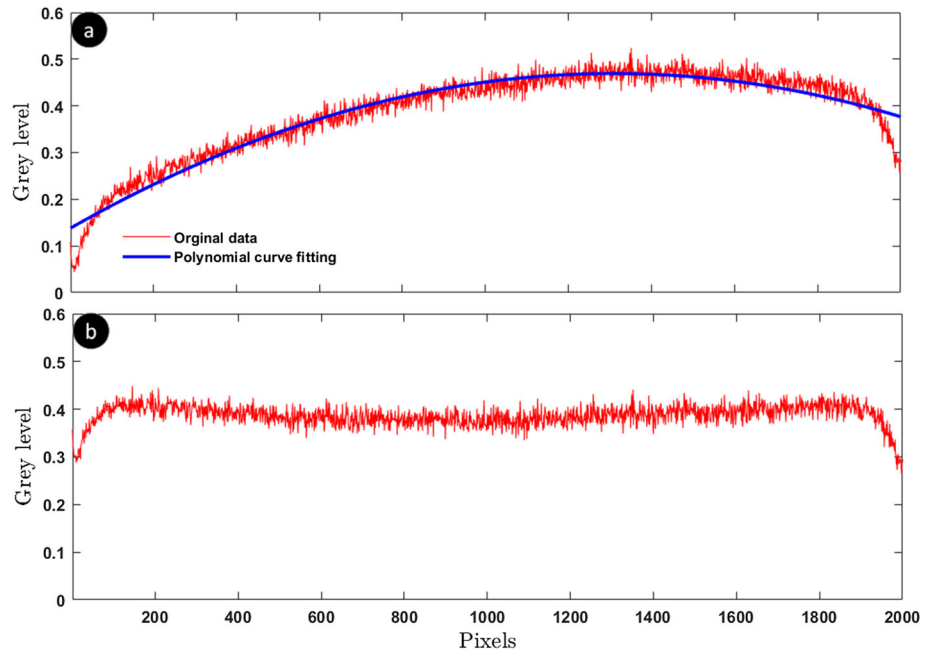

Fig. 6 Radiographic image of a steel sheet (**a**), examples of a row profile (**b**), and a column profile (**c**) underlying the anode heel effect

Fig. 7 Examples of curve fitting using a quadratic polynomial function (**a**), and the corresponding corrected profile (**b**)

where $\widehat{\mathbf{a}}$ is the vector of the optimal coefficients.

Then, the obtained vector **p** (the discrete form of the polynomial function P) is to be subtracted from $\mathbf{r_i}$. The last step is adding the mean of $\mathbf{r_i}$ to the subtraction result.

Hence, for a given original (*i.e.*, raw) radiographic image $\mathbf{R^o} = (r_{ij}^o)_{1 \leq i \leq M, \, 1 \leq j \leq N}$, the corrected image $\mathbf{R^c} = (r_{ij}^c)_{1 \leq i \leq M, \, 1 \leq j \leq N}$ can be obtained by calculating, for each row, the following formulae:

$$\mathbf{r_i^c} = \mathbf{r_i^o} - \mathbf{p} + \frac{1}{N} \sum_{j=1}^{N} r_{ij}^o, \ 1 \leq i \leq M \tag{8}$$

An example of a result is presented in Fig. 7, which shows the polynomial function P of the row profile given in Fig. 6b (Fig. 7a) and its corresponding corrected profile using Eq. 8 (Fig. 7b). As it can be noticed that the grey level is almost uniform except at the beginning and end of the data, where some trends can be observed. These trends can be due to the phenomena of scattering (diffraction), which occur at the edges of the specimen. Explicitly, when the X-rays come near the edges, they can be deflected from their original path due to the irregularity of the surface. This results in the divergence of X-rays in various directions, causing them to spread out and hence the decrease in grayscale levels (Bossi et al., 2002).

The edges, in this case, were abrupt, while WAAM specimens contain more smooth edges. Hence, the X-ray flux encounters a more gradual change in density, leading to a relatively lower amount of scattering compared to abrupt edges. Therefore, the impact of scattering is less severe.

Implementation

The methodology to implement the proposed approach is presented in Fig. 8. As it can be seen, the radiographic image ($\mathbf{R^o}$) and the 3D laser measurements data ($\mathbf{E^r}$) undergo, in the beginning, separate processing. The thickness measurements data are first corrected. Then, using the radiographic image of a step wedge, the relationship between the thickness and grey level is approximated using linear regression. Based on this function, the corrected thickness data ($\mathbf{E^c}$) are converted into a virtual radiographic image ($\mathbf{L}$). Concerning the radiographic image, the Heel effect is first corrected to mitigate the effect of the non-uniformity of the X-ray flux. Then, a matching is performed between the real radiographic image ($\mathbf{R^c}$) and the virtual one ($\mathbf{L}$), by visually determining the common part between the two images. Afterthat, $\mathbf{R^c}$ is resized, by applying a downsampling operation to match the dimensions of $\mathbf{L}$.

Once the two types of data are processed, $\mathbf{R^c}$ is subtracted from $\mathbf{L}$. Here, depending on the effects of defects on the grey level (*i.e.*, an increase or a decrease), the subtraction operation can result in negative and positive values. Therefore, two images can be derived from the obtained result, one keeping only the positive values of subtraction ($\mathbf{S^+}$) and the other keeping the negative values ($\mathbf{S^-}$). Mathematically, the result can be written as follows:

$$\mathbf{S}^\kappa = \begin{cases} s_{ij}^\kappa = \kappa \left(l_{ij} - r_{cij} \right) if \, s_{ij}^\kappa \in \mathbb{R}^\kappa \\ s_{ij}^\kappa = 0 \, else \end{cases}, \tag{9}$$
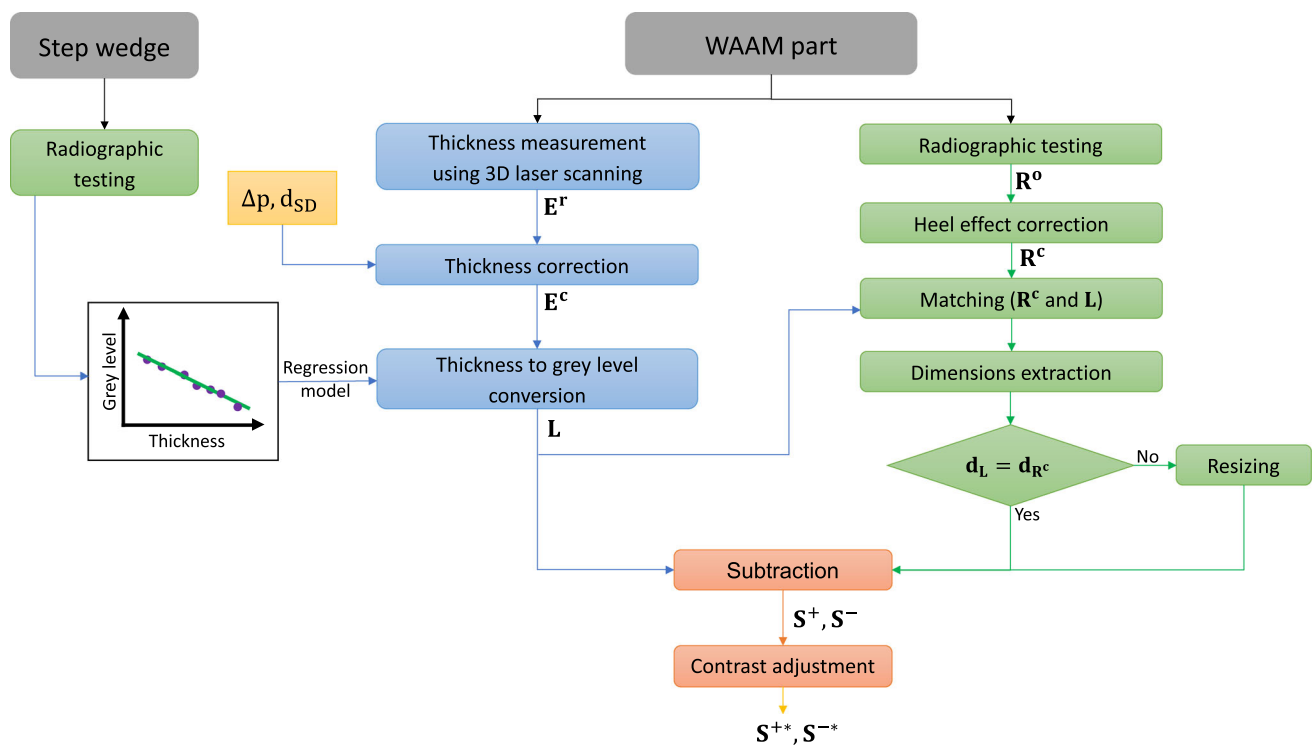
Fig. 8 Flowchart of the implementation of the proposed approach, $\mathbf{d_L}$ and $\mathbf{d_{R^c}}$ are the dimensions of the virtual and original radiographic images, respectively

where κ is the plus or the minus operator, $\mathbf{S}^\kappa = (s_{ij}^\kappa)_{i,j\in\mathbb{N}}$, $\mathbf{L} = (l_{ij})_{i,j\in\mathbb{N}}$, and $\mathbf{R^c} = (r_{ij}^c)_{i,j\in\mathbb{N}}$.

As mentioned earlier, the resulting image $\mathbf{S^+}$ should highlight defects generating an increase in the optical film density, such as the presence of porosities, lack of fusion or cracks. On this result, these defects will appear in white, and the healthy zones in black. While the resulting image $\mathbf{S^-}$ should highlight metallic inclusion type defects, for example tungsten used in inert gas tungsten (TIG) welding.

Applications

Weld bead

In order to test the efficiency of the proposed approach, a bead on a plate was considered. Firstly, a radiographic image of the bead and a step wedge was obtained. It is presented in Fig. 9a. Here, the image quality indicators (IQIs) were added to assess the quality of the resulting image. These indicators, which contain multiple wires of increasing diameter, are typically used in radiographic testing to evaluate the visibility of essential details in the radiographic image, especially the size and shape of the detectable discontinuities or defects (Solomon et al., 2013).

The weld bead heights were measured using a 3D laser system. The result is shown in Fig. 9b. The measured heights were then converted into grey level using the linear regression model shown in Fig. 9c. In this case, the value R^2 was around 0.99, which means that there is a strong linear correlation between the thickness and the grey level.

An example of a profile of $\mathbf{R^c}$ (green curve) and that of $\mathbf{L}$ (blue curve) crossing the weld are given in Fig. 9d. It can be noticed that the subtraction between the two profiles, shown also in Fig. 9d (red curve), is almost zero at the beginning because there is a perfect matching between the two curves. Then, some clear differences can be observed. They represent the hole drilled from the back wall of the plate along with the IQIs, which were added when performing radiographic testing. At the end of the two curves, a shift between them can also be noticed. This might be due to the abrupt change in the height of the weld seam after this position. The obtained results are presented in Fig. 10, which shows from top to bottom $\mathbf{R^c}$, $\mathbf{L}$, $\mathbf{S^+}$, and $\mathbf{S^-}$.

Visually, the grey level of the weld in $\mathbf{L}$ is very close to that of $\mathbf{R^c}$. Figure 10c is the resulting subtraction image $\mathbf{S^+}$. This figure shows that the weld is almost completely erased and highlights the differences between $\mathbf{R^c}$ and $\mathbf{L}$. We can clearly notice the IQIs that were added to the specimen. However, the dark cercle in $\mathbf{R^c}$ disappears in this result. This is because the result of subtraction is negative in this case.
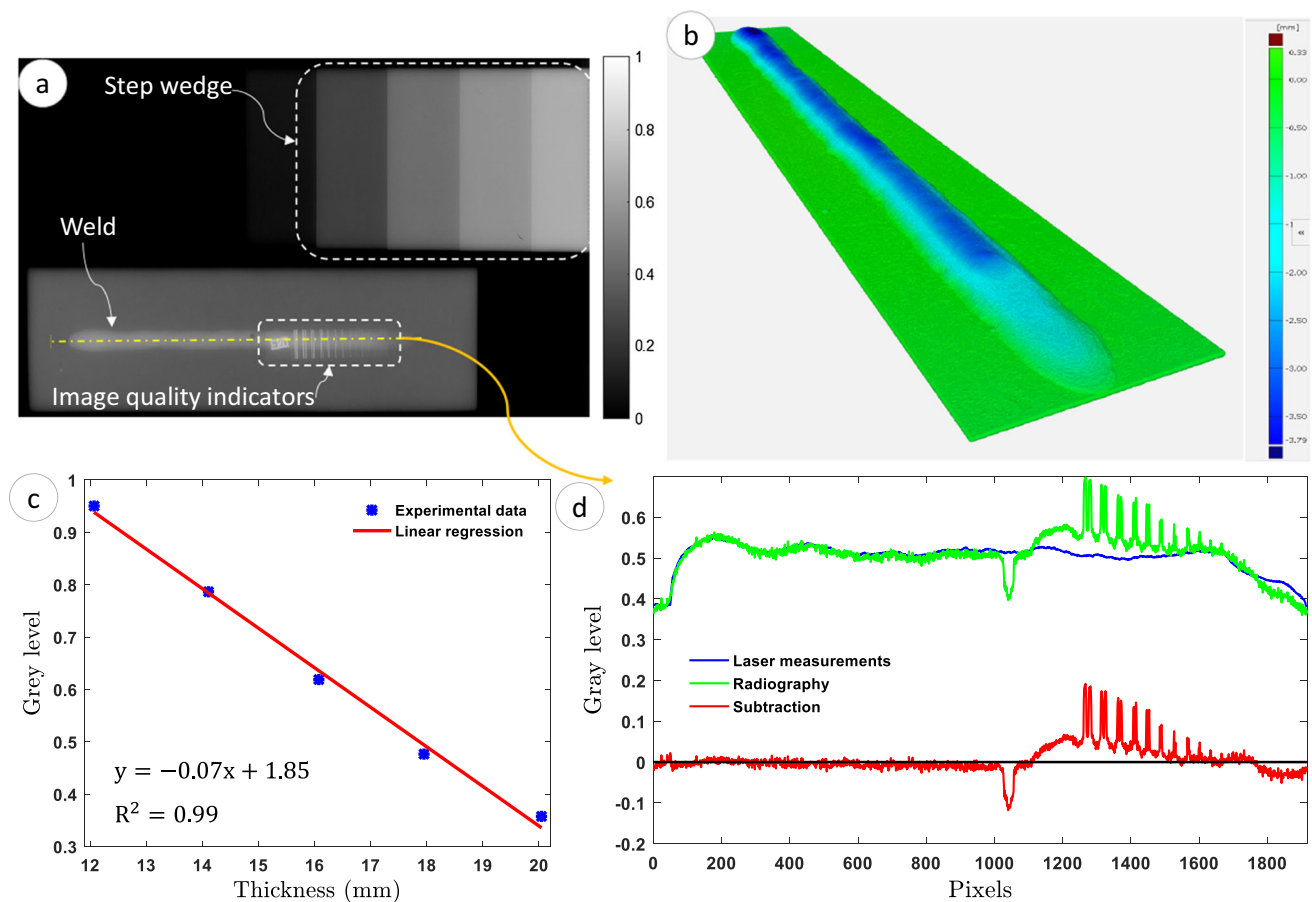
Fig. 9 Radiographic image of a weld bead (**a**), laser measurements (**b**), linear regression model (**c**), and result of the application of the proposed approach on a single profile (**d**)

Thus, it will rather appear in the complementary image (*i.e.*, resulting image $\mathbf{S}^-$) as it is shown in Fig. 10d. It can be remarked, however, that in $\mathbf{S}^-$, the weld seam is still visible. This is probably due to some errors, which include linear regression, scattering noise, etc.

WAAM walls

Manufacturing

Experimental configuration The considered WAAM specimens in this study are two walls with the following dimensions: 200 mm length, 100 mm width, and 20 mm height. The used robotic manufacturing cell is shown in Fig. 11. It is equipped with a KUKA KR30 robot, a KRC4 controller, and a TPS4000 generator with Cold Metal Transfer (CMT) technology (Selvi et al., 2018).

The used filler material is a C-Mn steel wire of type ER100S-G/G 69 4 M21 Mn3Ni1CrMo. Its chemical composition is shown in Table 1. The sheet used as baseplate is S355 steel with a thickness of 20 mm. It allows dissipation of the heat generated by the succession of deposits and ensures

a certain rigidity, which limits the deformations. Before each deposit, this baseplate was grinded to remove the oxide layer on the surface and then cleaned with acetone to remove all traces of grease.

Optimization of the deposition parameters The optimal manufacturing parameters are presented in Table 2. Some of these parameters were selected according to the filler material in order to obtain a stable arc and therefore, a regular deposit. The parameters that can have a significant impact on the geometry of the deposit are the wire feed rate and the deposition rate.

The methodology used to select the optimal deposition parameters is based on a trial-and-error approach. It is presented in Fig. 12. It consists in successively constructing single beads and small walls to validate the manufacturing parameters according to arc instabilities, lack of regularity, or the presence of defects. More precisely, the objective at the beginning is to weld a single bead with different wire feed and deposition rates to have different geometries (height and width). To do so, three values of wire feed rate were studied:
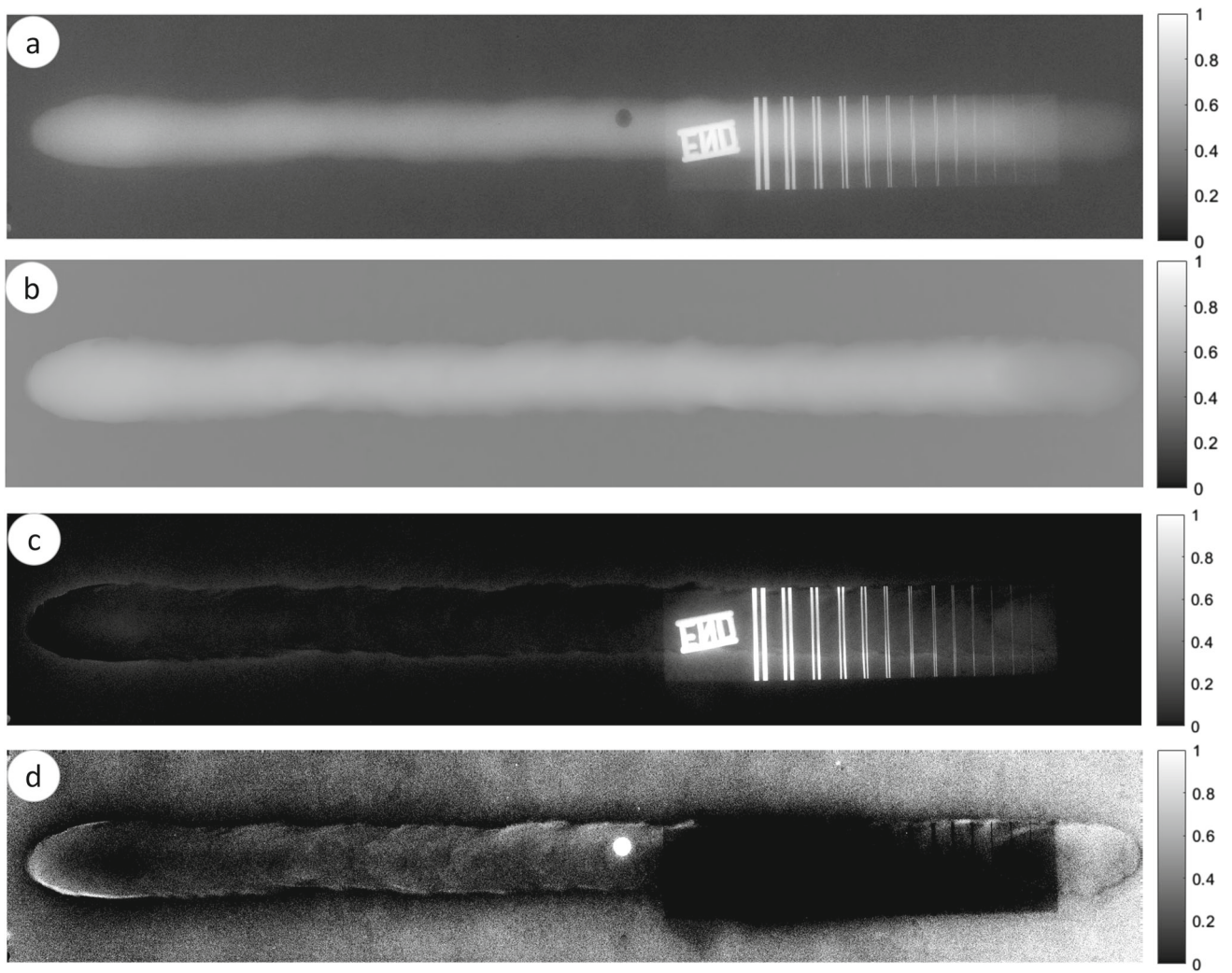
Fig. 10 Result of the application of the proposed approach on a weld bead: $\mathbf{R^c}$ (**a**), $\mathbf{L}$ (**b**), $\mathbf{S^+}$ (**c**), and $\mathbf{S^-}$ (**d**)
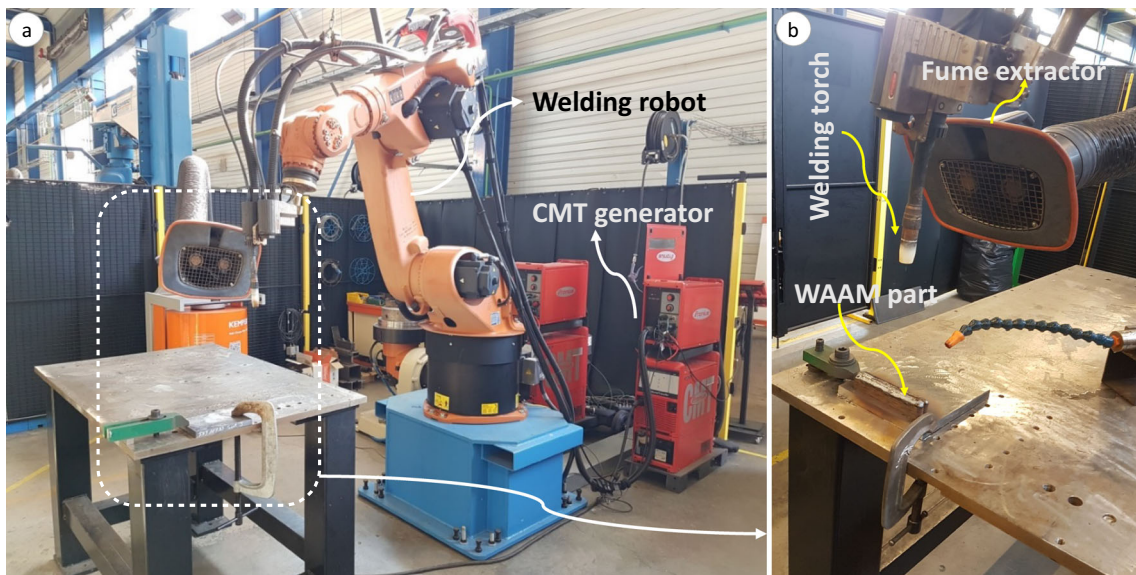
Fig. 11 WAAM robot (**a**), and zoom over the working table (**b**)

Table 1 Chemical composition of the filler material

Si	C	Mn	Cr	Ni	Mo	Cu	V	P	S	Ti	Zr	Al
0,6	0.08	1,6	0,3	1,4	0,25	0,15	0,08	0,01	0,01	0,002	0,002	0,005

Table 2 Manufacturing parameters

Synergy law	C1640
Stick-out	15 mm
Gaz flow	Ar + 20% CO_2/18 L/min
Temperature between layers	150 °C
Wire feed rate (m/min)	7.5
deposition rate (cm/min)	40

5, 7.5 and 10 m/min. The deposition rate values vary from 20 to 160 cm/min.

The characterization of each weld bead is done using a 3D laser scanner to determine its geometrical characteristics (*i.e.*, width and height of the bead). It is important to know here the relationship between the geometry of the weld bead and the deposition parameters to optimize the choice of these parameters.

Once the deposition parameters have been selected according to the geometry and regularity of a signal bead, they were tested for the manufacturing of small walls. The deposition strategy chosen to make the walls is a round trip in the longitudinal direction. It is composed of three passes per layer. This strategy, which is shown in Fig. 13, is alternated in each layer to improve the geometric regularity of the wall. Actually, the striking that causes an abundance of material balances the extinguishing, which produces a lack of material, and vice versa.

At this stage, the validation of the deposition parameters takes into account the presence of internal defects and the evolution of the geometry during manufacturing. Therefore, each layer is first characterized using a 3D laser scanner after its deposition. This allows to study the evolution of the top layer shape during the manufacturing process. Then, the wall is checked over multiple sections using macrographic analysis. The deposition parameters are considered as optimal if no defects are found on the different extracted sections.

Indeed, this approach for selecting optimal manufacturing parameters is time-consuming and costly. Nevertheless, with regard to the current state of the art, there is no other efficient method, which can be used for this purpose. Actually, this approach is still being used even in welding to establish the welding procedure specification (WPS). Different researchers have proposed to apply machine learning techniques to address this issue (Juang & Tarng, 2002; Xu et al., 2015; Zhang et al., 1996). The problem is that these techniques were performed in laboratory conditions and so they
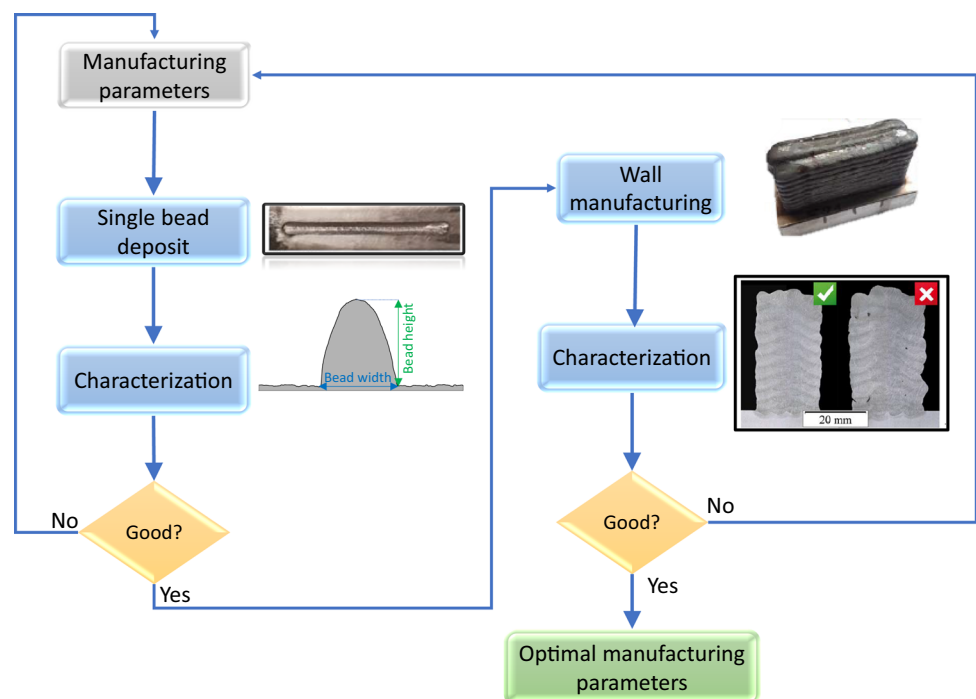

Fig. 12 Methodology to find the optimal manufacturing parameters

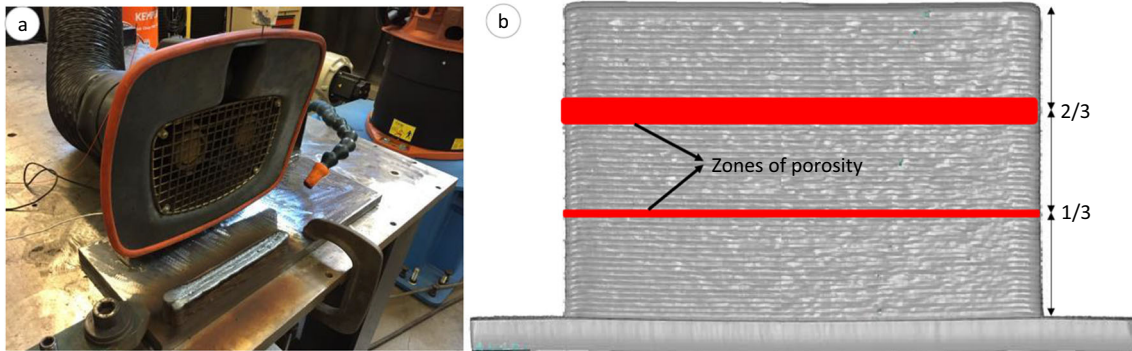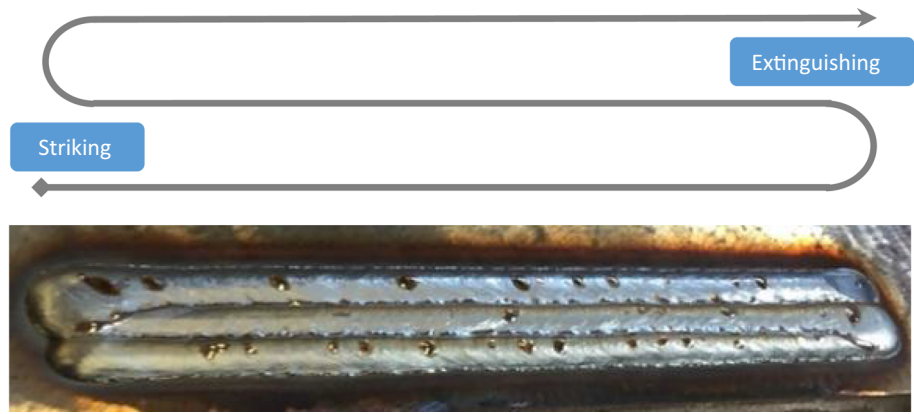**Fig. 13** Illustration of the manufacturing strategy

Fig. 14 Manufacturing a wall having defects: experimental setup (**a**), and porosities locations (**b**)

are difficult to embed in a production line as they require the construction of a database with complete characteristics of the welds (*i.e.*, welding parameters, geometrical and mechanical properties of the weld).

Defects creation The defects were obtained by altering the gas protection during deposition. To do so, the fume extractor was placed close to the deposition area as shown in Fig. 14(a). In this case, the air flow strongly disturbs the gas protection and results in arc instability and hence the occurrence of porosities.

These defects were created in two zones of the wall: at 1/3 and 2/3 of its height as shown in Fig. 14b. In the first zone (located at 1/3), the fume extractor was only activated during the deposition of the central bead of the layer and during deposition of two consecutive layers. Thus, the beads located on the edges do not have any disturbance of the gas protection. Concerning the second zone (located at 2/3), the fume extractor was activated during the deposition of the whole layer and during the deposition of two consecutive layers.

Testing

Defect-free wall A defect-free wall, shown in Fig. 15a, was obtained using the found optimal manufacturing parameters. As it can be noticed, the top-right corner was machined to add a step wedge. Radiographic testing was performed over this specimen using the parameters shown in Table 3. Then, the obtained radiographic film was digitized with a resolution of 50 μm. The result is shown in Fig. 15b. 3D laser measurements were also performed on this specimen. The result is presented in Fig. 15c.

Wall with intentional defects The proposed approach has been also applied on a second wall that contains intentional defects namely, porosities. The manufactured wall is shown in Fig. 16a. The radiographic parameters were kept the same as for the healthy wall except the use of a D3 detector with a time exposure of 13 min. The obtained X-ray film was then digitized, and the result is given in Fig. 16b. After that, the 3D laser scanning was performed in order to measure the surface profile of the specimen. The result is presented in Fig. 16c.
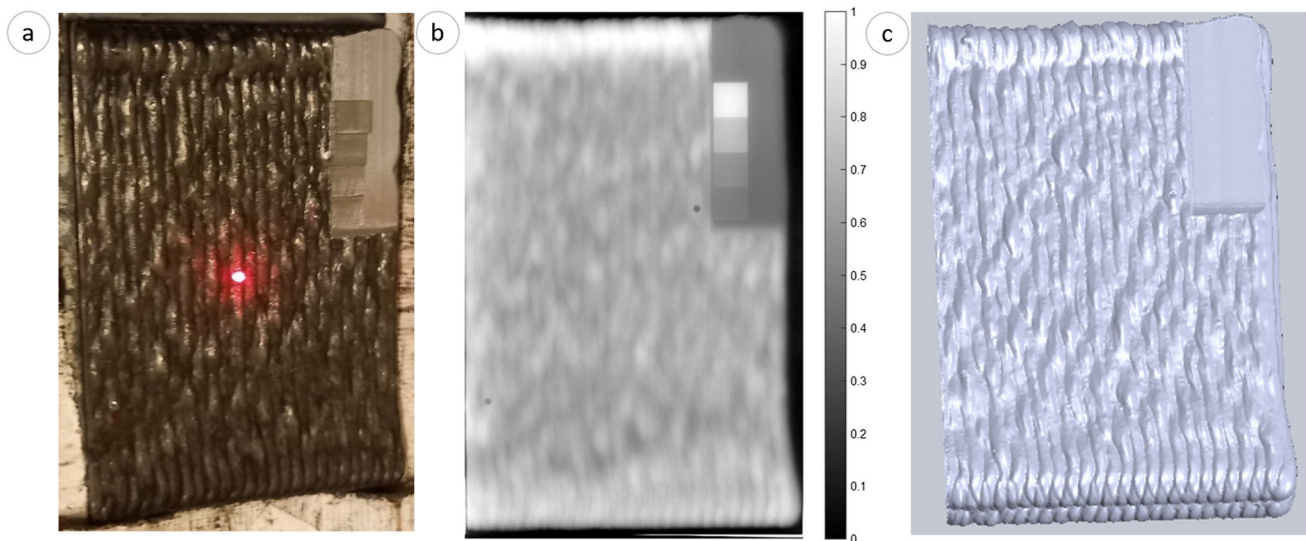
Fig. 15 Defect-free wall: Photography (**a**), its radiographic image (**b**), and its 3D laser scanning image (**c**)

Table 3 Parameters of radiographic testing

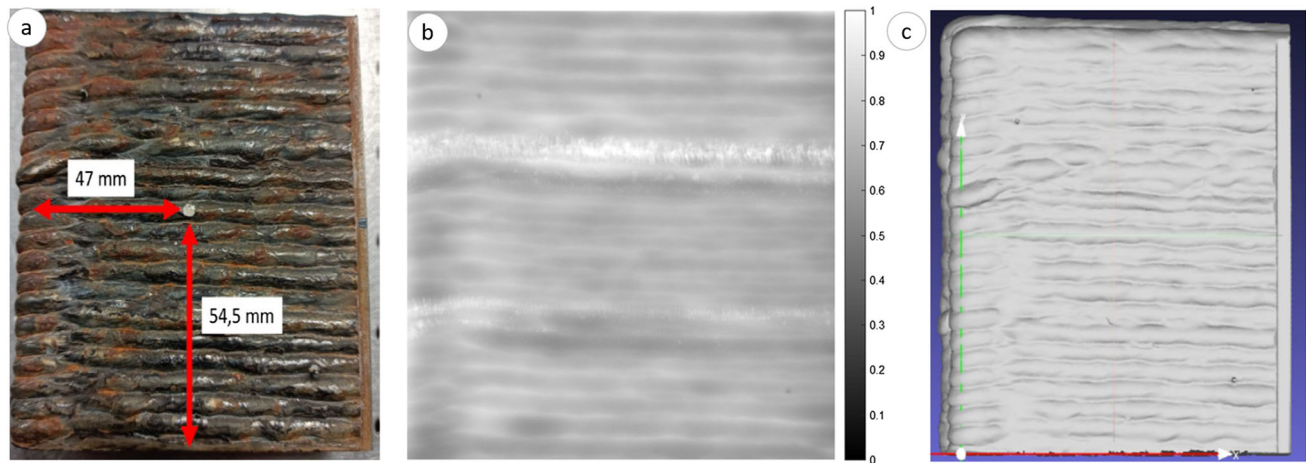| Current	Voltage	Source-detector Distance	Exposure time	Pre-filter	Filter	Detector
4.5 mA	200 kV	700 mm	7 min	1.5 mm Cu	0.2 mm Pb	Agfa D4

Fig. 16 Second manufactured wall: Photography (**a**), its radiographic image (**b**), and its 3D laser scanning image (**c**)

It is important to note here that to enable perfect matching between radiographic image and 3D measurement image, a small rod was added to the surface of the specimen on two different diametrically opposed positions.

To avoid machining the part of the specimen containing the step wedge as in the case of the defect-free wall, radiographic testing of step wedge was performed separately. However, using the same operational parameters, the radiographic result was not satisfactory. Actually, the signal saturation masks the separation between the step wedge levels. It was found that the main parameter that improves the result is the exposure time. Figure 17 shows the obtained results for three different exposure time.

Application of the proposed approach

Defect-free wall The real radiography ($\mathbf{R^e}$) and the virtual one ($\mathbf{L}$) of the defect-free wall are given in Fig. 18a and
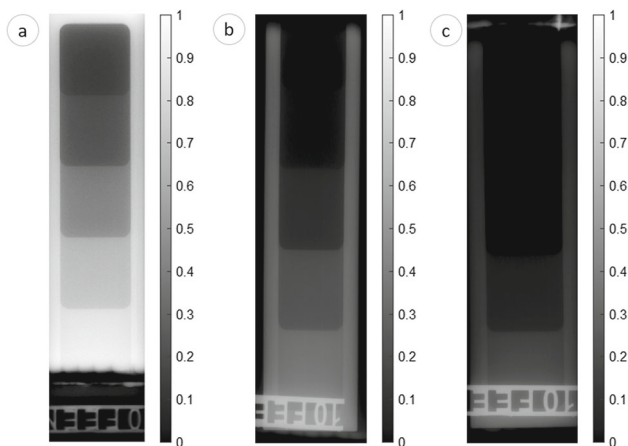
Fig. 17 Influence of the exposure time on the result of radiographic testing of a step wedge: 10 min (**a**), 11 min (**b**), and 13 min (**b**)

b, respectively. The image $\mathbf{R^c}$ seems to be blurry comparatively to $\mathbf{L}$. One possible reason for this difference is the phenomenon of scattering in radiographic testing. Besides, the two drilled holes in the specimen, clearly shown in $\mathbf{R^c}$, are not properly presented in $\mathbf{L}$. Actually, the one on the top-right is not shown and the one on the bottom-left is represented by white spot which indicates that measuring errors happened at this position.

A profile from the images $\mathbf{R^c}$ and $\mathbf{L}$ along with the result of subtraction are shown in Fig. 18c. This result shows that, at this position where the profiles were taken, a nearly perfect match is noticed between the two profiles except near the edges. The green curve shows the result of subtraction, which is very close to zero.

The subtraction results between $\mathbf{R^c}$ and $\mathbf{L}$ are presented in Fig. 19. Figure 19a represents the resulting image $\mathbf{S^+}$. As

expected, the grey level is almost uniform for the whole specimen except the machined corner where the step wedge was added and some white random spots that are due to measuring errors when performing 3D laser scanning. As a reminder, this specimen was manufactured using optimal manufacturing parameters. It is supposed thus to be free of defects.

The resulting image $\mathbf{S^-}$ is presented in Fig. 19b. Unlike $\mathbf{S^+}$, this result presents some features that are probably due to an overestimation of the relationship between the thickness of the specimen and the grey level.

Wall with intentional defects Concerning the second wall, the $\mathbf{R^c}$ image is shown in Fig. 20a. After converting the measured thicknesses using 3D laser scanner into grey level values, the resulting image $\mathbf{L}$ is shown in Fig. 20b. Clear differences between the images can be noticed especially for the second position of defects (*i.e.*, location 2/3 shown in Fig. 14b). However, as in the previous example, it can be noticed that $\mathbf{R^c}$ is blurry than $\mathbf{L}$. Besides, the grey level of $\mathbf{L}$ is relatively brighter than that of $\mathbf{R^c}$. This issue is probably due to the data of the step wedge used in the linear regression as the exposure time was not the same for the specimen.

Figure 20c shows a profile extracted from $\mathbf{R^c}$ and $\mathbf{L}$ crossing the two positions of defects. The blue profile is obtained from real radiography and the red one from the virtual radiography. In the beginning, the two profiles seem to be perfectly matched that's why the result of subtraction (*i.e.,* green curve) is close to zero. At the first position of defect, a change of behaviors between the two curves can be noticed. At the end, an overestimation of the values of thickness is observed. This results in subtraction errors.

The results of subtraction are shown in Fig. 21. In the resulting image $\mathbf{S^+}$, the positions of defects are clearly highlighted. This is because the surface roughness is significantly
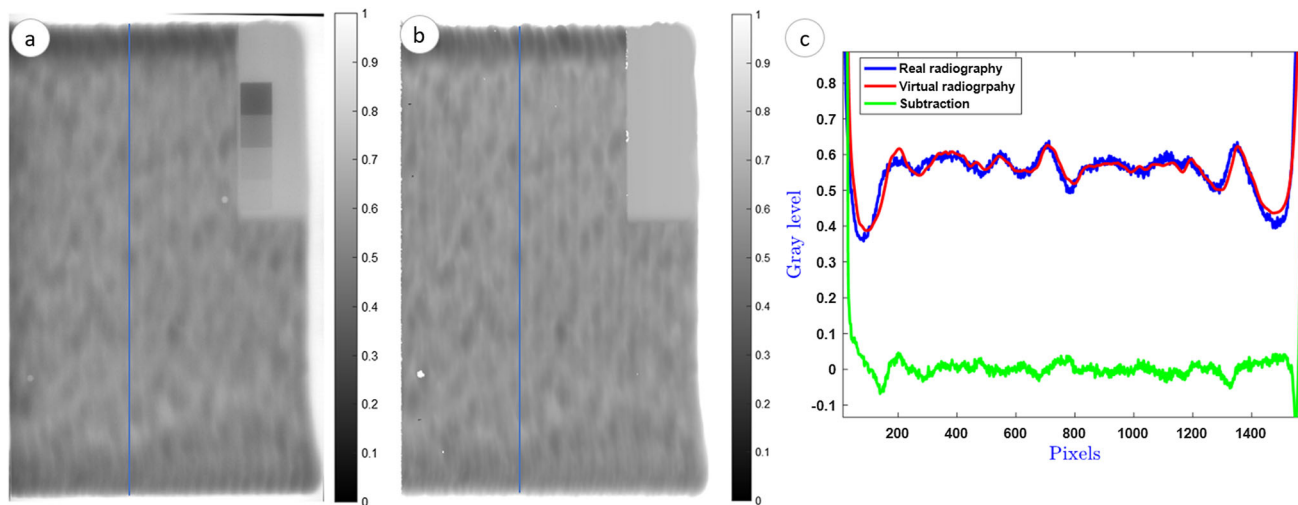

Fig. 18 Defect-free wall: $\mathbf{R^c}$ (**a**), $\mathbf{L}$ (**b**) and profiles obtained from $\mathbf{R^c}$ and $\mathbf{L}$ along with the result of subtraction (**c**)

Fig. 19 Results after application of the proposed approach on a defect-free wall: $\mathbf{S}^+$ (**a**), and $\mathbf{S}^-$ (**b**)
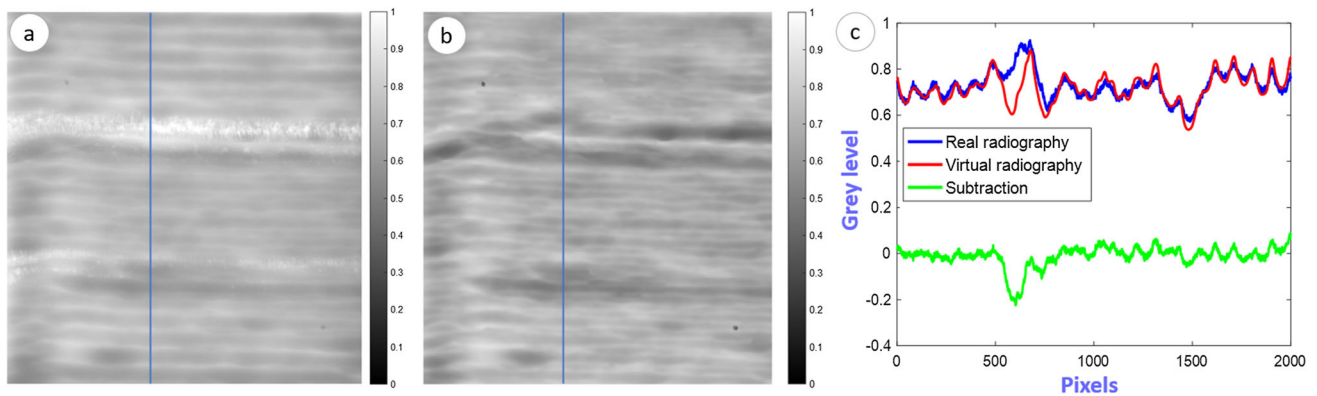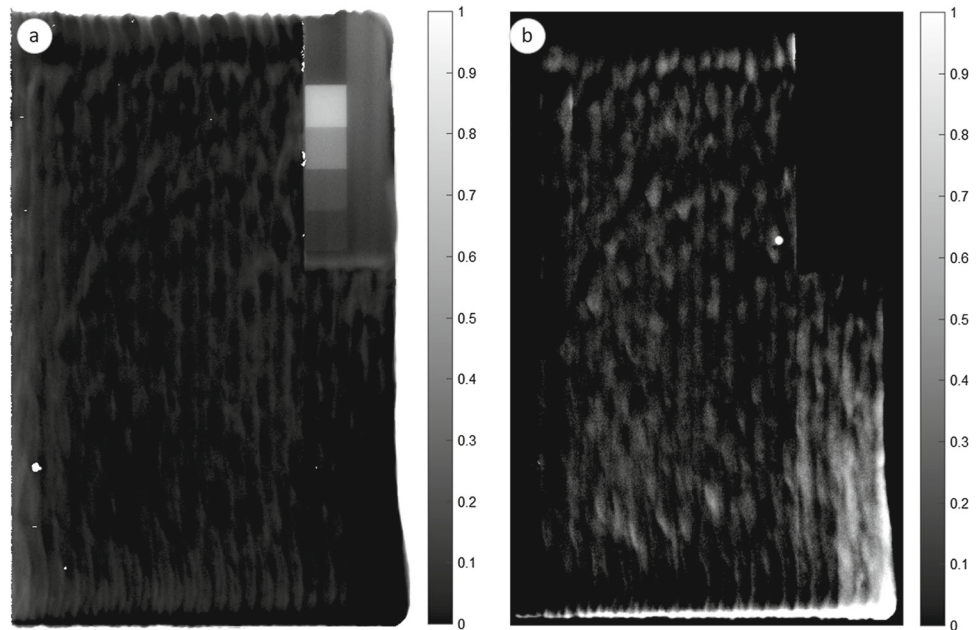

Fig. 20 Wall with intentional defects: $\mathbf{R}^c$ (**a**), $\mathbf{L}$ (**b**), and profiles obtained from $\mathbf{R}^c$ and $\mathbf{L}$ along with the result of subtraction (**c**)

mitigated. However, in the result $\mathbf{S}^-$, the representation of the surface roughness remains visible except for the first position of defects where these patterns are barely visible. In the second position of defects, some porosities can be noticed in black color.

In order to clearly quantify the added value of proposed processing approach, two curves representing the sum of the rows of $\mathbf{R}^c$ and that of $\mathbf{S}^+$ were first obtained. These curves, presented in Fig. 22, show that the presence of defects induces large variation of the amplitude in the case of the processed data, especially for the second defect zone.

Then, a statistical measure called detectability index (DI) was derived, which can be written as follows:

$$\mathrm{DI} = \frac{\sigma \, (\text{defective zone})}{\sigma \, (\text{healhty zone})}, \qquad (10)$$

where σ is the standard deviation.

The healthy zone was fixed at the first 150 values, the same window (*i.e.*, 150 values) was taken for the defective zones. The results are depicted in Table 4. They show that the standard variation of the amplitudes of the first defective zone for processed data is almost four times bigger than that of the healthy zone while for the original, this value is almost the same, which means that statistically, it is difficult to discriminate between the healthy and defect zones in this case. Concerning the second defective zone, the standard deviation of the amplitudes for the processed data is almost 27 times compared to the healthy zone while it is only 2 times for the original data.

Validation

To evaluate the effectiveness of the proposed approach, a comparison with other NDT methods namely phased array ultrasonic testing and computed tomography was performed.
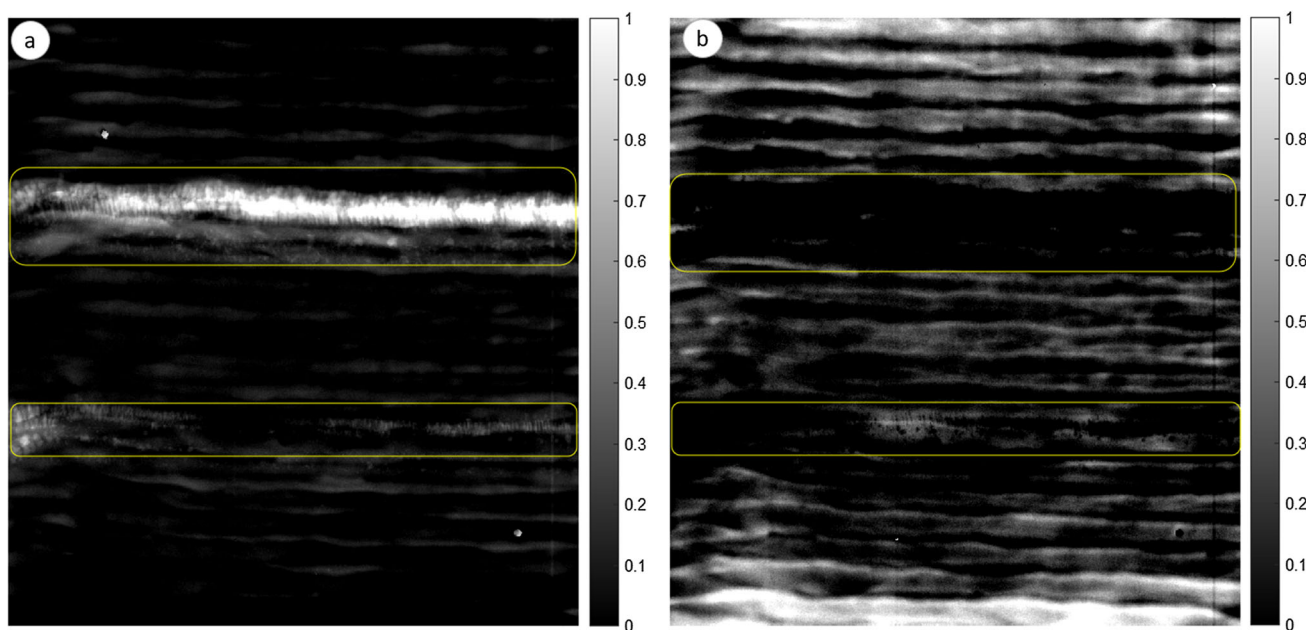
Fig. 21 Results after application of the proposed approach on the second manufactured wall: S^+ (**a**), and S^- (**b**)

Fig. 22 Comparison between the result of defect detection using original data and processed data. These curves were obtained by summing the rows of R^c and that of S^+
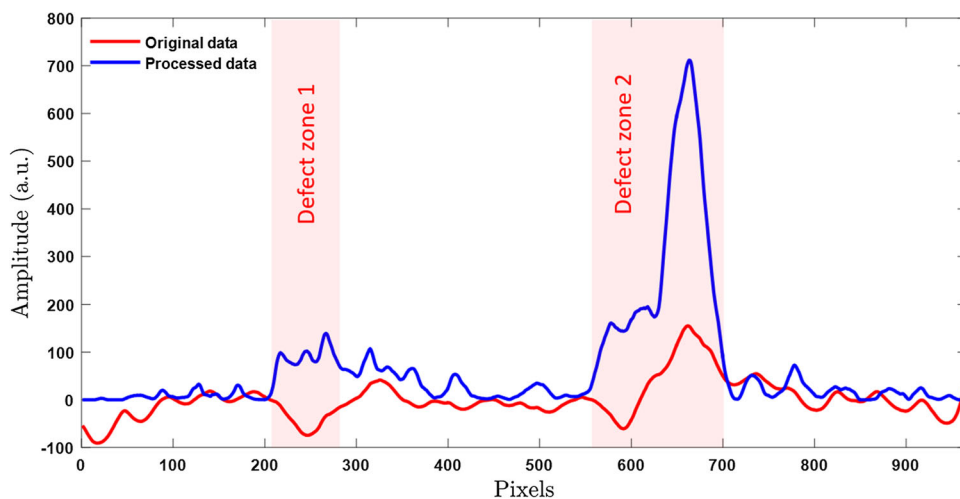

Table 4 Results of the detectability index of the two identified zones of defect

	Processed data	Original data
DI (defect zone 1)	3.61	1.03
DI (defect zone 2)	27.55	2.00

Phased array ultrasonic testing Phased array (PA) ultrasonic testing is a very popular NDT technique used to inspect and evaluate the integrity of materials and structures. It employs multiple ultrasonic elements arranged in a phased array probe, allowing for the generation of ultrasonic beams that can be focused and steered electronically. The received signals are used to generate a visual representation of the internal structure of the material.

In order to enable the application of this technique in our case (*i.e.*, avoid the constraint of surface irregularities), the scanning was performed from the substrate side as shown in Fig. 23a. The characteristics of the used PA probe are given in Table 5.

The result is shown in Fig. 23b. As it can be seen, the two lines of the intentionally created defects are clearly shown. It is worth noting here that for the ease of interpretation of this result, the interface and backwall echoes were removed.
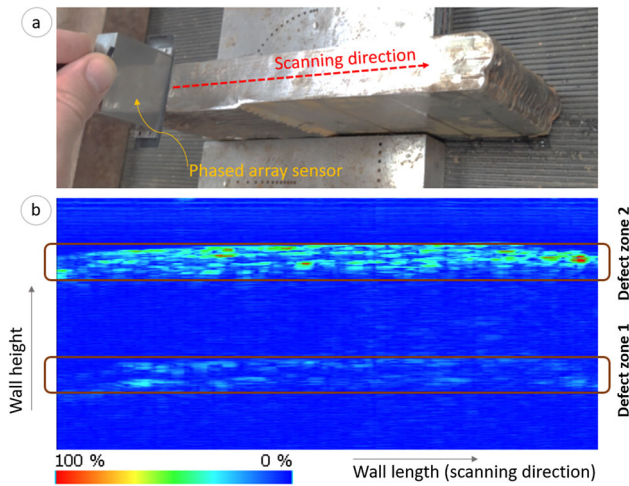
Fig. 23 Result of defect detection using phased array ultrasonic technique applied on the second manufactured wall

Computed tomography X-ray computed tomography was applied on the same wall. Details about the working principles of this technique and its application to additive manufacturing parts are discussed in (Khosravani & Reinicke, 2020).

In the present work, a specific acquisition procedure was used. Actually, the projections obtained at certain angular positions during the 360° rotation leading to high crossed thickness were not taken into account for the reconstruction. To enable a clear look on the inside of the specimen, cross-section areas at different positions were extracted. The results are presented in Fig. 24. These results confirm the positions where the defects were intended to be created and show the distribution of the porosities at these positions.

Table 5 Characteristics of the used PA probe

Manufacturer	Type	Frequency (MHz)	Number of elements	Inter-element distance (mm)	Height (mm)
IMASONIC	Linear arrays	5	64	0.1	10
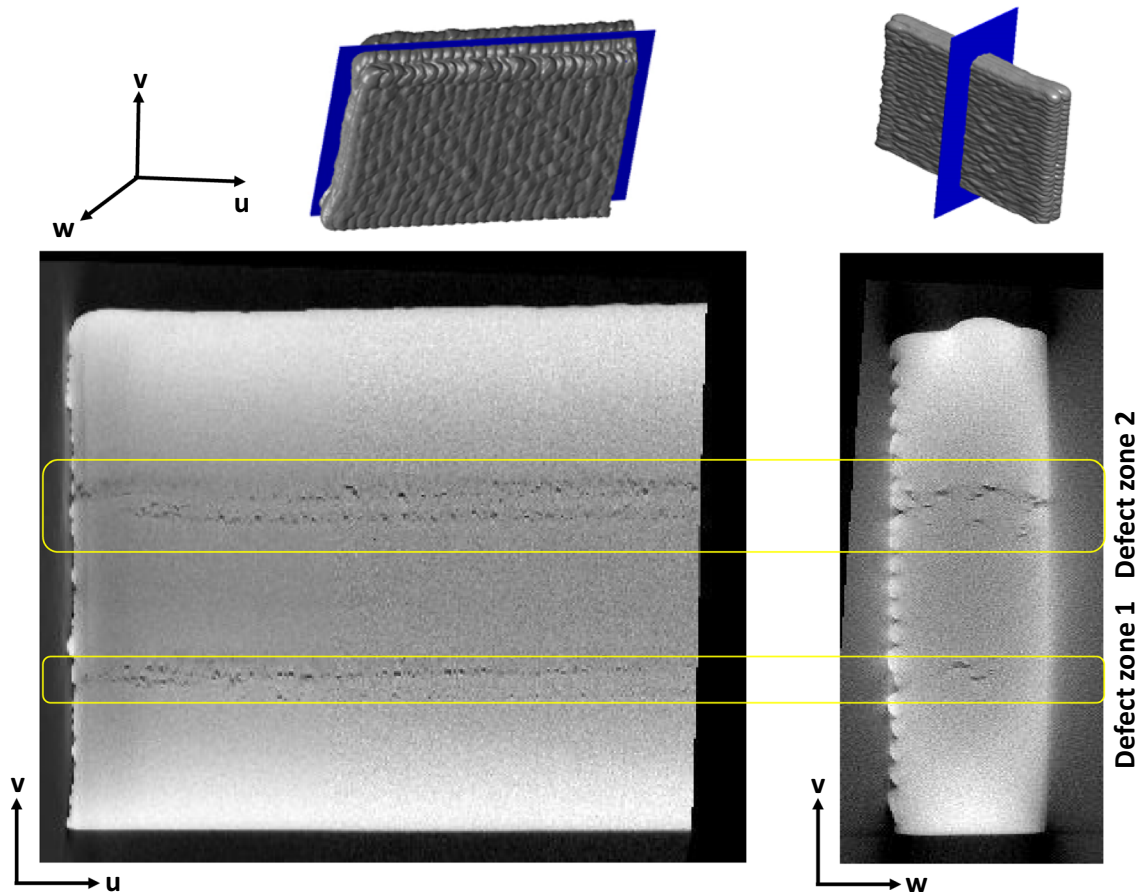
Fig. 24 Tomography results obtained from the wall with intentional defects

Conclusions and perspectives

This paper proposed a novel approach to improve defect detectability and interpretation of radiographic testing results on WAAM parts. The approach involves measuring the thickness of the part using a 3D laser scanner and converting these values into grey level image. Then, subtracting the digitized real radiographic image of the specimen from the obtained image.

One of the significant advantages of this proposed approach is that it eliminates the need for grinding or milling to perform radiographic testing. While the results obtained were promising, some improvements are still required to mitigate the effects of the scattered photons. Besides, special attention has to be paid to the range of thickness provided by the step wedge to construct the linear regression model. This range should include the range of thickness of the WAAM parts. Otherwise, the constructed model could give inaccurate estimate of the gray level for a given thickness.

Future work will focus on optimizing the operational parameters in radiographic testing by increasing the source energy to mitigate the effect of scattered photons. In addition, digital radiography will be applied since the digital detectors exhibit a linear response as a function of the exposure, which should result in a more reliable relationship between the thickness and the observed gray level. Furthermore, image processing techniques based on feature recognition will be employed to ensure automatic matching between the original and the virtual radiographic images.

References

Behiels, G., Maes, F., Vandermeulen, D., & Suetens, P. (2002). Retrospective correction of the heel effect in hand radiographs. *Medical Image Analysis, 6*(3), 183–190. https://doi.org/10.1016/S1361-8415(02)00078-6

Bevans, B., Ramalho, A., Smoqi, Z., Gaikwad, A., Santos, T. G., Rao, P., & Oliveira, J. P. (2023). Monitoring and flaw detection during wire-based directed energy deposition using in-situ acoustic sensing and wavelet graph signal analysis. *Materials and Design, 225*, 111480. https://doi.org/10.1016/j.matdes.2022.111480

Bossi, R. H., Iddings, F. A., & Wheeler, G. C. (2002). *Radiographic Testing*. Berlin: American Society for Nondestructive Testing.

Chabot, A., Laroche, N., Carcreff, E., Rauch, M., & Hascoët, J. Y. (2020). Towards defect monitoring for metallic additive manufacturing components using phased array ultrasonic testing. *Journal of Intelligent Manufacturing, 31*(5), 1191–1201. https://doi.org/10.1007/s10845-019-01505-9

Chauveau, D. (2018). Review of NDT and process monitoring techniques usable to produce high-quality parts by welding or additive manufacturing. *Welding in the World, 62*(5), 1097–1118. https://doi.org/10.1007/s40194-018-0609-3

Chen, X., Kong, F., Fu, Y., Zhao, X., Li, R., Wang, G., & Zhang, H. (2021). A review on wire-arc additive manufacturing: Typical defects, detection approaches, and multisensor data fusion-based model. *International Journal of Advanced Manufacturing Technology, 117*(3–4), 707–727. https://doi.org/10.1007/s00170-021-07807-8

Cheng, C. L., & Shalabh, & Garg, G. (2014). Coefficient of determination for multiple measurement error models. *Journal of Multivariate Analysis, 126*, 137–152. https://doi.org/10.1016/j.jmva.2014.01.006

Cunningham, C. R., Flynn, J. M., Shokrani, A., Dhokia, V., & Newman, S. T. (2018). Invited review article: Strategies and processes for high quality wire arc additive manufacturing. *Additive Manufacturing, 22*(June), 672–686. https://doi.org/10.1016/j.addma.2018.06.020

Derekar, K. S. (2018). A review of wire arc additive manufacturing and advances in wire arc additive manufacturing of aluminium. *Materials Science and Technology (united Kingdom), 34*(8), 895–916. https://doi.org/10.1080/02670836.2018.1455012

Do Nascimento, M. Z., Frère, A. F., & Germano, F. (2008). An automatic correction method for the heel effect in digitized mammography images. *Journal of Digital Imaging, 21*(2), 177–187. https://doi.org/10.1007/s10278-007-9072-1

He, X., Wang, T., Wu, K., & Liu, H. (2021). Automatic defects detection and classification of low carbon steel WAAM products using improved remanence/magneto-optical imaging and cost-sensitive convolutional neural network. *Measurement: Journal of the International Measurement Confederation, 173*, 108633. https://doi.org/10.1016/j.measurement.2020.108633

Honarvar, F., & Varvani-Farahani, A. (2020). A review of ultrasonic testing applications in additive manufacturing: Defect evaluation, material characterization, and process control. *Ultrasonics, 108*(February), 106227. https://doi.org/10.1016/j.ultras.2020.106227

Huang, C., Wang, G., Song, H., Li, R., & Zhang, H. (2022). Rapid surface defects detection in wire and arc additive manufacturing based on laser profilometer. *Measurement: Journal of the International Measurement Confederation, 189*, 110503. https://doi.org/10.1016/j.measurement.2021.110503

Javadi, Y., MacLeod, C. N., Pierce, S. G., Gachagan, A., Lines, D., Mineo, C., et al. (2019). Ultrasonic phased array inspection of a Wire + Arc Additive Manufactured (WAAM) sample with intentionally embedded defects. *Additive Manufacturing, 29*, 1–20. https://doi.org/10.1016/j.addma.2019.100806

Juang, S. C., & Tarng, Y. S. (2002). Process parameter selection for optimizing the weld pool geometry in the tungsten inert gas welding of stainless steel. *Journal of Materials Processing Technology, 122*(1), 33–37. https://doi.org/10.1016/S0924-0136(02)00021-3

Khosravani, M. R., & Reinicke, T. (2020). On the use of X-ray computed tomography in assessment of 3D-printed components. *Journal of Nondestructive Evaluation*. https://doi.org/10.1007/s10921-020-00721-1

Kusk, M. W., Jensen, J. M., Gram, E. H., Nielsen, J., & Precht, H. (2021). Anode heel effect: Does it impact image quality in digital radiography? *A Systematic Literature Review. Radiography, 27*(3), 976–981. https://doi.org/10.1016/j.radi.2021.02.014

Lee, S. S., & Kim, Y. H. (2005). Validation of protocols for corrosion and deposits determination in small diameter. *International Atomic Energy Agency*, 71–79. Retrieved March 10, 2023, from https://www.iaea.org/publications/7128/development-of-protocols-for-corrosion-and-deposits-evaluation-in-pipes-by-radiography

Lee, C., Seo, G., Kim, D. B., Kim, M., & Shin, J.-H. (2021). Development of defect detection AI model for wire + arc additive

manufacturing using high dynamic range images. *Applied Sciences, 11*(16), 7541. https://doi.org/10.3390/app11167541

Li, Y., Polden, J., Pan, Z., Cui, J., Xia, C., He, F., et al. (2022). A defect detection system for wire arc additive manufacturing using incremental learning. *Journal of Industrial Information Integration, 27*, 100291. https://doi.org/10.1016/j.jii.2021.100291

Lopez, A., Bacelar, R., Pires, I., Santos, T. G., Sousa, J. P., & Quintino, L. (2018). Non-destructive testing application of radiography and ultrasound for wire and arc additive manufacturing. *Additive Manufacturing, 21*(January), 298–306. https://doi.org/10.1016/j.addma.2018.03.020

Ma, Y., Hu, Z., Tang, Y., Ma, S., Chu, Y., Li, X., et al. (2020). Laser opto-ultrasonic dual detection for simultaneous compositional, structural, and stress analyses for wire + arc additive manufacturing. *Additive Manufacturing, 31*(November), 100956. https://doi.org/10.1016/j.addma.2019.100956

Misale, V. N., Ravi, S., & Narayan, R. (2009). on non-destructive evaluation digital radiography systems techniques and performance evaluation for space applications. In *Proceedings of the National Seminar & Exhibition on Non-Destructive Evaluation* (pp. 172–176).

Munaro, M., So, E. W. Y., Tonello, S., & Menegatti, E. (2015). Efficient completeness inspection using real-time 3D color reconstruction with a dual-laser triangulation system. In *Integrated Imaging and Vision Techniques for Industrial Inspection: Advances and Applications* (pp. 201–225). https://doi.org/10.1007/978-1-4471-6741-9_7

Nazemi, E., Movafeghi, A., Rokrok, B., & Dastjerdi, M. H. C. (2019). A novel method for predicting pixel value distribution non-uniformity due to heel effect of X-ray tube in industrial digital radiography using artificial neural network. *Journal of Nondestructive Evaluation*. https://doi.org/10.1007/s10921-018-0542-9

Omiyale, B. O., Olugbade, T. O., Abioye, T. E., & Farayibi, P. K. (2022). Wire arc additive manufacturing of aluminium alloys for aerospace and automotive applications: A review. *Materials Science and Technology (united Kingdom), 38*(7), 391–408. https://doi.org/10.1080/02670836.2022.2045549

Pawluczyk, O., & Yaffe, M. J. (2001). Field nonuniformity correction for quantitative analysis of digitized mammograms. *Medical Physics, 28*(4), 438–444. https://doi.org/10.1118/1.1359244

Ramalho, A., Santos, T. G., Bevans, B., Smoqi, Z., Rao, P., & Oliveira, J. P. (2022). Effect of contaminations on the acoustic emissions during wire and arc additive manufacturing of 316L stainless steel. *Additive Manufacturing*. https://doi.org/10.1016/j.addma.2021.102585

Salleh, H., Samat, S. Bin, Matori, M. K., Jamal, M., Isa, M., Arshad, M. R., et al. (2014). Heel Effect: Dose Mapping and Profiling for Mobile C-Arm Fluoroscopy Unit Toshiba Sxt-1000a. In *R&D Seminar: Research and Development, Malaysia*. Retrieved March 10, 2023, from https://inis.iaea.org/search/search.aspx?orig_q=RN:46091401

Selvi, S., Vishvaksenan, A., & Rajasekar, E. (2018). Cold metal transfer (CMT) technology - An overview. *Defence Technology, 14*(1), 28–44. https://doi.org/10.1016/j.dt.2017.08.002

Shin, S. J., Hong, S. H., Jadhav, S., & Kim, D. B. (2023). Detecting balling defects using multisource transfer learning in wire arc additive manufacturing. *Journal of Computational Design and Engineering, 10*(4), 1423–1442. https://doi.org/10.1093/jcde/qwad067

Solomon, J. B., Li, X., & Samei, E. (2013). Relating Noise to image quality indicators in CT examinations with tube current modulation. *American Journal of Roentgenology, 200*(3), 592–600. https://doi.org/10.2214/AJR.12.8580

Surovi, N. A., & Soh, G. S. (2023). Acoustic feature based geometric defect identification in wire arc additive manufacturing. *Virtual and Physical Prototyping*. https://doi.org/10.1080/17452759.2023.2210553

Tennakoon, T. M. R. (2005). Validation of protocols for corrosion and deposit determination in pipes by radiography "CORDEP". *International Atomic Energy Agency,* 81–84. Retrieved March 10, 2023, from https://www.iaea.org/publications/7128/development-of-protocols-for-corrosion-and-deposits-evaluation-in-pipes-by-radiography

Thompson, G. T., & Balch, S. J. (1988). An efficient algorithm for polynomial curve fitting. *Computers and Geosciences, 14*(5), 547–556. https://doi.org/10.1016/0098-3004(88)90016-7

Wang, T. W., & Evans, J. P. O. (2021). Stereoscopic Dual-energy X-ray Imaging for Target Materials Identification. *In: IEE Proceedings - Vision Image and Signal Processing*, (May 2003), 205–212. https://doi.org/10.1049/ip-vis:19990158

Williams, S. W., Martina, F., Addison, A. C., Ding, J., Pardal, G., & Colegrove, P. (2016). Wire + Arc additive manufacturing. *Materials Science and Technology (united Kingdom), 32*(7), 641–647. https://doi.org/10.1179/1743284715Y.0000000073

Xu, W. H., Lin, S. B., Fan, C. L., & Yang, C. L. (2015). Prediction and optimization of weld bead geometry in oscillating arc narrow gap all-position GMA welding. *International Journal of Advanced Manufacturing Technology, 79*(1–4), 183–196. https://doi.org/10.1007/s00170-015-6818-7

Yaacoubi, S., El Mountassir, M., Ferrari, M., & Dahmene, F. (2019). Measurement investigations in tubular structures health monitoring via ultrasonic guided waves: A case of study. *Measurement: Journal of the International Measurement Confederation, 147*, 106800. https://doi.org/10.1016/j.measurement.2019.07.028

Zhang, Y. M., Kovacevic, R., & Li, L. (1996). Characterization and real-time measurement of geometrical appearance of the weld pool. *International Journal of Machine Tools and Manufacture, 36*(7), 799–816. https://doi.org/10.1016/0890-6955(95)00083-6

Zimermann, R., Mohseni, E., Lines, D., Vithanage, R. K. W., MacLeod, C. N., Pierce, S. G., et al. (2021). Multi-layer ultrasonic imaging of as-built Wire + Arc Additive Manufactured components. *Additive Manufacturing, 48*, 102398. https://doi.org/10.1016/j.addma.2021.102398